Charge transport and yield variations in electron-beam irradiated insulators

Behrouz Raftari,[1] Neil Budko,[1] and Kees Vuik[1]
Delft Institute of Applied Mathematics, Delft University of Technology, Mekelweg 4, 2628 CD Delft, The Netherlands

(Dated: 1 August 2016)

In this paper the space-time evolution of free and trapped charge densities and the variations of the secondary electron yield in electron-beam irradiated insulators are investigated with the help of a self-consistent drift-diffusion-reaction model. It is shown that focused high-current low-energy beams create quasi-stationary shock-type distributions of trapped charges leading to characteristic charging patterns around the injection point. Simulations also reproduce and clarify the origins of such phenomena as the drop/increase of the secondary electron yield to unity and the electrostatic mirroring effect. Analysis shows that the quality and proximity of the ground contact, the recombination velocity of the sample surface, and the transient nature of the yield may help to explain the apparent differences in the shapes of yield curves observed in various experiments.

PACS numbers: 77.84.Bw, 79.20.Ap, 79.20.Hx, 72.20.Jv, 02.60.Cb, 02.70.Dh
Keywords: Drift-diffusion-reaction; Electron-beam irradiated insulators; Surface potential; Secondary electron emission

I. INTRODUCTION

Charge transport and trapping in insulators have long been studied due to their importance in such areas as memory-based technologies, electron multipliers, ceramic surfaces, industrial cables, and the safety of spacecraft[1–4]. The focus of many of these studies is on the charging of insulators irradiated by electrons. Also, while a scanning electron microscope is a very powerful tool, its application to the investigation of insulators is limited due to difficulties in the interpretation of image brightness and various image distortions typically attributed to sample charging.

Probably, the earliest systematic studies of electron-irradiation effects in solids and charge trapping and transport in insulators, as parts of research on electrets, were carried out by Bernhard Gross who has had a great impact on this research field. In his seminal works on irradiation phenomena[5,6] Gross investigated the electron trapping and charge buildup in high-resistivity solid insulators bombarded with energetic electrons. Further studies by Gross and coworkers produced new experimental techniques and mathematical models[7–10].

These and more recent[11,12] studies have been carried out with two purposes. The first is to eliminate the charging effect, which, of course, can also be achieved by simply coating the sample with a conductive surface layer. The second goal is the theoretical understanding of the underlying mechanisms responsible for the charging. In spite of the considerable amount of theoretical work carried out, no single approach has yet been able to provide a complete and coherent account of all observed phenomena[13,15–17,49]. This could be due to the prevailing emphasis on static (stationary) models and the secondary yield rather than the internal charge dynamics[18–20]. The existing dynamic (continuum) models are either one-dimensional[13,49] or do not include some of the relevant physical processes (e.g. dynamic recombination, trapping, etc.)[16,17]. This is why the Monte-Carlo (MC) simulations[21] are still considered to be the golden standard, even though these MC models become computationally very expensive and unreliable when the long-rage electrostatic interaction and the long-time dynamic behavior are considered. These were some of the original reasons behind the development of the present self-consistent drift-diffusion-reaction (DDR) model[22].

Previously[22] we have shown that the DDR model can handle single PE impacts as well as continuous current irradiation and that it reproduces the SE yield at a chosen primary electron (PE) energy in accordance with experimental data. The only tuning parameter (in the absence of relevant data) is the sample-vacuum surface recombination velocity (SRV). Considering a single-impact irradiation may well be a stretch of the applicability limits for continuum models (due to a small number of SE's produced in a single impact). Yet, the results obtained for many consecutive impacts were in good agreement with the continuous current source and provided an intuitively compelling picture.

Further validation of the DDR method against experimental data for a range of PE energies is complicated by the fact that the published yield-energy curves even for the most typical insulators such as silica and alumina often do not agree with each other, and the corresponding experimental setups are not documented in sufficient detail. Moreover, SEM practitioners report different yields obtained with the same sample under different irradiation conditions (zoom factor, beam current, etc.). One of the goals of the present paper is to understand the reasons behind these discrepancies and outline the major factors that might be influencing the SE yield. To do so we have performed simulations on a much larger temporal scale than in[22] and for a much broader range of parameters. In particular, this allowed us to notice the emergence of quasi-stationary shocks in the distribution of trapped charges at higher beam currents, which, for

obvious reasons, could not be seen with the previous 1D continuum models and MC simulations.

Apart from the trapped-charge shocks, among the main results we can mention the identification of the quality and proximity of the ground contact as one of the most important factors, the detailed analysis of the various stages in the time evolution of the yield, and the explicit demonstration that the trapping process, which slows down DDR simulations, may be neglected when considering the steady-state yield.

After a brief recap of the DDR method in Section II, Section III presents our analysis of the trapped charge dynamics. Section IV focuses on the comparison with the experimental yield-energy data, reproduction of known charging phenomena (unity yield, mirroring effect, etc.), and investigation of the possible reasons behind the yield variations.

II. DDR MODEL AND ITS IMPLEMENTATION

In this section we recall the main features of the DDR model and describe several improvements that have been implemented since its introduction in[22]. The continuum approximation of the equilibrium transport of charged particles in insulators consists of both partial (PDE) and ordinary (ODE) differential equations augmented with a semi-empirical source function accounting for the initial ballistic transport stage. The PDE's are the Poisson equation for the potential and the transport equations for the free charge density:

$$-\nabla\cdot(\varepsilon\nabla V)=\frac{q}{\varepsilon_0}(p+p_t-n-n_t), \tag{1}$$

$$\frac{\partial n}{\partial t}+\nabla\cdot\mathbf{J}_n=U+\frac{j_0}{q}g_n-\frac{\partial n_t}{\partial t}, \tag{2}$$

$$\frac{\partial p}{\partial t}+\nabla\cdot\mathbf{J}_p=U+\frac{j_0}{q}g_p-\frac{\partial p_t}{\partial t}, \tag{3}$$

with the constitutive relations for the current densities given by

$$\mathbf{J}_n=-D_n\nabla n+\mu_n n\nabla V, \tag{4}$$

$$\mathbf{J}_p=-D_p\nabla p-\mu_p p\nabla V, \tag{5}$$

where q is the elementary charge, $V(\mathbf{x},t)$ is the electrostatic potential, $n(\mathbf{x},t)$ is the density of free electrons, $n_t(\mathbf{x},t)$ is the density of trapped electrons, $p(\mathbf{x},t)$ is the density of free holes, $p_t(\mathbf{x},t)$ is the density of trapped holes, the constant ε_0 is the dielectric constant of vacuum, the function $\varepsilon(\mathbf{x})$ is the (static) relative permittivity of the sample, μ_n and μ_p are the electron and hole mobilities, j_0 is the primary beam current, D_n and D_p are the diffusion coefficients, g_n and g_p are the distributions of charge pairs per primary incident electron based on a semi-empirical formula[23] and described in detail in[22], and U is the charge recombination rate given below (8).

The two nonlinear ODE's are the following trap rate equations:

$$\frac{\partial n_t}{\partial t}=\begin{cases}\sigma_n\upsilon_{th}(N_n-n_t)(n-n_i)-\gamma_n n_t, & \text{if } n\geq n_i,\\ -\gamma_n n_t, & \text{otherwise,}\end{cases} \tag{6}$$

$$\frac{\partial p_t}{\partial t}=\begin{cases}\sigma_p\upsilon_{th}(N_p-p_t)(p-n_i)-\gamma_p p_t, & \text{if } p\geq n_i,\\ -\gamma_p p_t, & \text{otherwise,}\end{cases} \tag{7}$$

where σ_n and σ_p are the electron and hole trapping cross sections, γ_n and γ_p are the detrapping time constants, N_n and N_p are the densities of trapping sites, υ_{th} is the thermal velocity, and n_i is the intrinsic carrier density. These equations have been modified here to prevent nonphysical detrapping when $n_t<N_n$ and $n<n_i$ and/or $p_t<N_p$ and $p<n_i$.

We continue using the well-known Shockley-Read-Hall (SRH) model[24] for the recombination rate:

$$U(n,p)=\frac{n_i^2-np}{\tau_n(n+n_i)+\tau_p(p+n_i)}, \tag{8}$$

where τ_n and τ_p are the life time parameters for the electrons and holes, respectively.

The initial conditions on n and p at $t=0$ are set as the corresponding intrinsic carrier densities of the materials under consideration. The source functions in (2)–(3) are switched on at $t=0$ and contain the distribution function of the charge pairs at the end of the initial ballistic stage:

$$g_{n,p}(\mathbf{x},E_{\text{lan}})=\left(A\frac{E_{\text{lan}}}{E_{\text{i}}}+B\right)\frac{1}{\pi R^3}\exp\left(-\frac{7.5}{R^2}|\mathbf{x}-\mathbf{x}_0|^2\right) \tag{9}$$

where $E_{\text{lan}}=E_0+V_{\text{s}}$ is the effective landing energy of electrons, E_0 is the energy of PE's in the electron beam, and V_s is the surface potential, E_{i} is the pair creation energy, and A is the constant corresponding to the backscattering rate. In the hole distribution function g_p the constant B is zero, however, it is different from zero in the electron distribution function g_n accounting for the remaining PE's. The maximum penetration depth of the primary electrons R is given by the following semi-empirical formula[25]:

$$R(\rho,E_{\text{lan}})=93.4\frac{E_{\text{lan}}^{1.45}}{\rho^{0.91}}\ [\text{nm}], \tag{10}$$

where $\mathbf{x}_0$ is the center of the Gaussian distribution with the distance of $0.3R$ from the sample-vacuum interface.

In the first set of numerical experiments we consider an inhomogeneous sample consisting of an insulator on

top of a semiconductor substrate. Specifically, we look at an alumina (or silica) half-sphere (or short vertical cylinder) on top of a silicon layer, since this has been a typical target in many papers[26,27]. Figure 1 shows the vertical cross-section of the target, where the cylinder is indicated by a dashed contour. In the second set of numerical experiments we consider a more basic setup, the vertical cross-section of which is shown in Fig. 10.

In this paper we devote significant attention to the influence of boundary conditions on charge transport. Three types of boundary conditions are of relevance to the present problem: Dirichlet, Neumann, and Robin. The unknown quantities of interest – V, n, p – may obey different boundary conditions in different situations.

For example, the Dirichlet boundary condition on the free charge densities n and p at the side of the computational domain means that the sample has an ohmic contact there, i.e., any excess or lack of free charge will be quickly extinguished or replenished by charges that are assumed to be in infinite supply at the ohmic contact. The Dirichlet boundary condition for the electric potential means that the value of the potential is maintained at the boundary, e.g., positive potential at the detector or zero potential at the 'ground' electrode. The Neumann boundary condition means that the normal derivative of the corresponding quantity is fixed at the boundary. If the Neumann condition on n or p is homogeneous (derivative is zero), then there will be no diffusion-driven flux of n or p through that boundary. If the Neumann condition on V is homogeneous, then there will be no drift-driven flux of n and p through that boundary.

For the vacuum-sample interface we use the following slightly modified version of the Robin-type boundary condition proposed in[22]:

$$\mathbf{J}_n \cdot \nu = \begin{cases} v_n(n - n_i^I) & \text{on} \quad n \geq n_i^I, \\ 0 & \text{otherwise,} \end{cases} \text{ on } \Sigma \times [0, t_{\text{end}}], \tag{11}$$

$$\mathbf{J}_p \cdot \nu = 0 \text{ on } \Sigma \times [0, t_{\text{end}}]. \tag{12}$$

It acts as a semi-insulating contact for the electrons and an insulating contact for the holes. The parameter v_n is the surface recombination velocity (SRV) of electrons at vacuum-sample interface, n_i^I is the intrinsic carrier density of the insulator and ν denotes the unit outward normal vector on the boundary Σ.

The first step toward obtaining a numerical solution of an equation or a system of equations is to investigate the existence and uniqueness of the solution. With regards to the present model, the consistency analysis relies on previously published results. A detailed investigation concerning the existence and uniqueness of stationary drift-diffusion equations can be found in[24]. In a study conducted by Jerome[28] a mathematical analysis of a system solution map for the weak form of the DDR model, which forms a basis for the numerical solution of the model, has been provided. Also, in a follow-up study by Busenberg et al.[29] the wellposedness of a DDR model similar to the present one (with different source/sink terms) has been demonstrated.

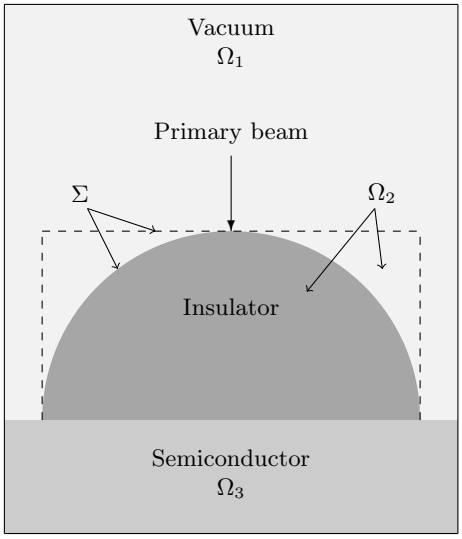

FIG. 1. Vertical cross-section of the domain. The object is an insulating half-sphere (or a cylinder – shown as dashed line) on top of a semi-conducting layer, irradiated from above by a focused electron beam.

The multiscale nature of the problem calls for the same strategy as was used in[22] regarding the scaling of variables. We apply the finite element method (FEM) for the numerical solution of the model equations and implement it as a solver within the COMSOL Multiphysics package. To balance the accuracy and the computational costs a careful strategy is needed. Our investigations show that the best (i.e., most reliable) results are obtained when we use adaptive (or local) mesh refinement, second-order Lagrange shape functions, the fully coupled approach with the Newton-Raphson solver, and an adaptive time-stepping algorithm. The use of the adaptive grid refinement, although costly, alleviates the need for more sophisticated approaches, such as the traditional exponential fitting applied in semiconductor studies[30,31].

Although it is possible to perform actual 3D simulations with the present model, it would require a relatively large amount of memory and time. As we have found out 3D computations become much faster if the trapping rate equations (6)–(7) are omitted. Hence, one of the purposes of the present paper is to acquire a good qualitative understanding of their effect on the solution with the goal to find a simpler model that would be more feasible in 3D. In the present case, however, the geometry, boundary conditions, and the source are all axially symmetric, so that the original 3D problem can be reduced to a 2D problem in the (r, z)-plane of the cylindrical coordinate system.

III. EVOLUTION OF TRAPPED-CHARGE DENSITIES

In this section we describe an unusual phenomenon that, in particular, causes a significant slow-down of DDR simulations and requires adaptive (or local) grid refinement in the presence of the trapping rate equations (4)–(5). Namely, the emergence of quasi-stationary shock-like distributions in the density of trapped electrons for a certain range of PE energies and beam currents. Physically, these shocks may result in a ring of positive charge surrounding the injection point and remaining on the surface of insulators for a very long time after the electron beam has been switched off.

In principle, a propagating electron shock wave is expected to occur under certain conditions in collision-dominated processes, such as the electron production, drift, and diffusion. However, so far this phenomenon has been observed mostly in plasmas and also semiconductors described by hydrodynamic models (e.g. Boltzmann equation)[32–35], and to our best knowledge there has been no discussion/observation of shocks in the context of solid insulators. Moreover, shocks reported here are stationary rather than moving, and concern trapped rather than free charges.

Since at the moment we are far from having a full explanation of this phenomenon, in what follows we shall simply present our simulations, outline the conditions under which the shock occurs, and suggest a way to confirm its existence experimentally. Another goal of this work is to establish the conditions under which the shock *does not* occur, so that the DDR simulations can be simplified and performed on a larger scale.

A. Influence of beam current and energy

We begin by assessing the role of the beam current (i.e. charge concentration in the impact zone) in the creation of lateral shocks. Consider a sample consisting of Al_2O_3 half-sphere with the radius of 100 nm on top of a grounded silicon substrate (see Fig. 1).

Figure 2 shows the time evolution of electron and hole trapped-charge densities inside the Al_2O_3 half-sphere irradiated by a a 200 pA beam of 1 keV electrons. The densities represent slowly moving wave fronts, eventually reaching the silicon substrate, so that after about 100 μs both densities are completely uniform within the half-sphere. This means that all trapping sites have been occupied and the effect of trapped charges on the evolution of free charges reduces to additional relatively weak and spatially uniform source terms, whose rate is governed by the corresponding detrapping rates. The effective mobility increases, since particles are no longer being lost to trapping. It is also interesting to note that with equal trapping sites densities $N_n = N_p$ the resulting distributions of trapped electrons and trapped holes completely neutralize each other. In fact, we have observed that even with $N_n \neq N_p$ the excess of trapped charges is mostly neutralized (apart from the interfaces, perhaps) by attracting the opposite free charges, if the latter are supplied in sufficient numbers by the source or via an ohmic contact.

Computationally, much of the mesh refinement work is caused by these slowly moving, but very sharp trapped-charge wave fronts. Therefore, when all trapping sites are occupied one can study the late-time dynamics of free charges without the two trapping rate equations (6)–(7) by introducing two additional source terms in (2)–(3), thus, making the problem computationally much less expensive and 3D-feasible.

The moving trapped-charge wave fronts in Fig. 2 have two interesting features. First, the concentration of particles behind the fronts is almost uniformly equal to the trapping sites densities, i.e., $n_t \approx N_n$ and $p_t \approx N_p$, whereas, in front of the wave the trapped-charge densities are almost uniformly close to zero. Hence, one-dimensionally these waves look almost like step functions. Second, the trapped-holes wave has a thin and fast precursor that runs along the surface of the half-sphere towards the silicon substrate. Whereas, the trapped-electrons wave, on the contrary, bends backwards along the interface. We believe that this is caused by the excess of free holes and the lack of free electrons that are available for trapping near the sample/vacuum interface, since free electrons can leave the sample, while free holes can not. The effect could also be reinforced by the reduced recombination rate within the shock zone.

Although beam currents of a typical SEM are in the order of hundreds of pA at most, higher beam currents are also being used[36,37]. For instance, the beam current of 200 nA has been reported in a multi-beam SEM[38]. With higher currents the aforementioned lack of trapped electrons at the interface takes the form of a shock (lateral with respect to the beam direction) as can be seen in Fig. 3, where the beam currents of 20 and 200 nA have been simulated. This shock appears to stabilize as soon as the slow trapped-particles density wave reaches the grounded silicon substrate. As mentioned above, all trapping sites are occupied behind the trapped-particles wave fronts. Hence, when these fronts reach the substrate an efficient transport channel for free electrons and holes is created connecting the impact zone, the sample/vacuum interface, the silicon substrate, and the ohmic ground contact.

Figure 4 presents the relative density of trapped electrons n_t/N_n along the spherical sample/vacuum interface (starting from the top). The plots show the snapshots from the time evolution of n_t/N_n at 1, 10, and 100 μs for different beam currents, corresponding to the images of Figures 2, 3. These plots demonstrate the eventual disappearance of the shock at lower beam currents and its relatively stable shape at higher beam currents. Also, the leftmost boundary of the shock, i.e., the distance from the injection point to the shock zone becomes smaller with increasing beam current.

As far as other quantities of interest are concerned, in

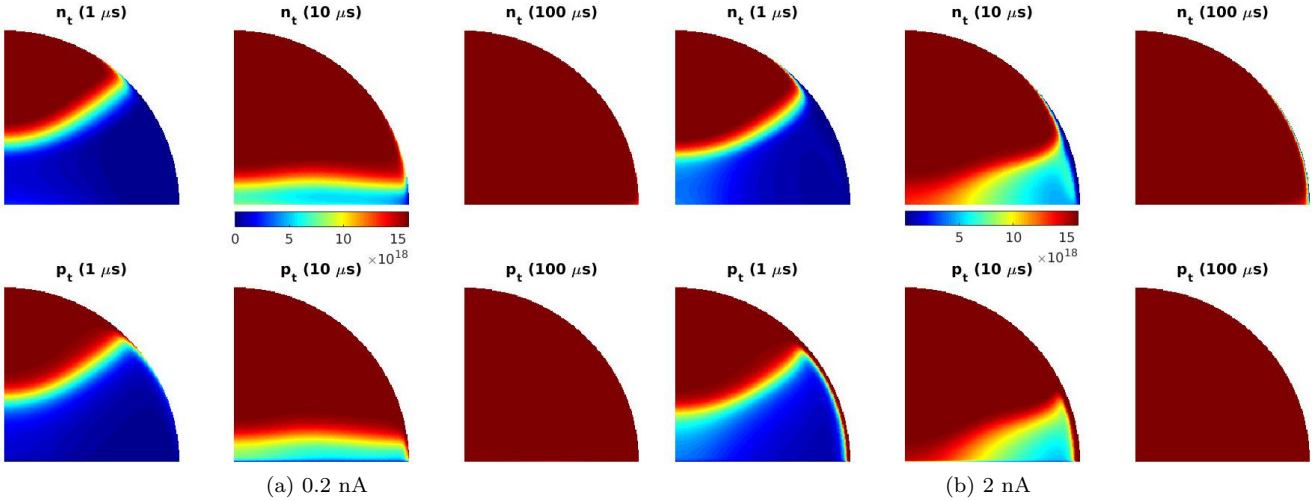

(a) 0.2 nA (b) 2 nA

FIG. 2. Densities of trapped electrons (top row) and trapped holes (bottom row) in Al_2O_3 half-sphere at 1, 10, and 100 μs since the start of irradiation by focused 200 pA **(a)** and 2 nA **(b)** beams of 1 keV PE's. At this current/energy levels the shock is either absent or temporary.

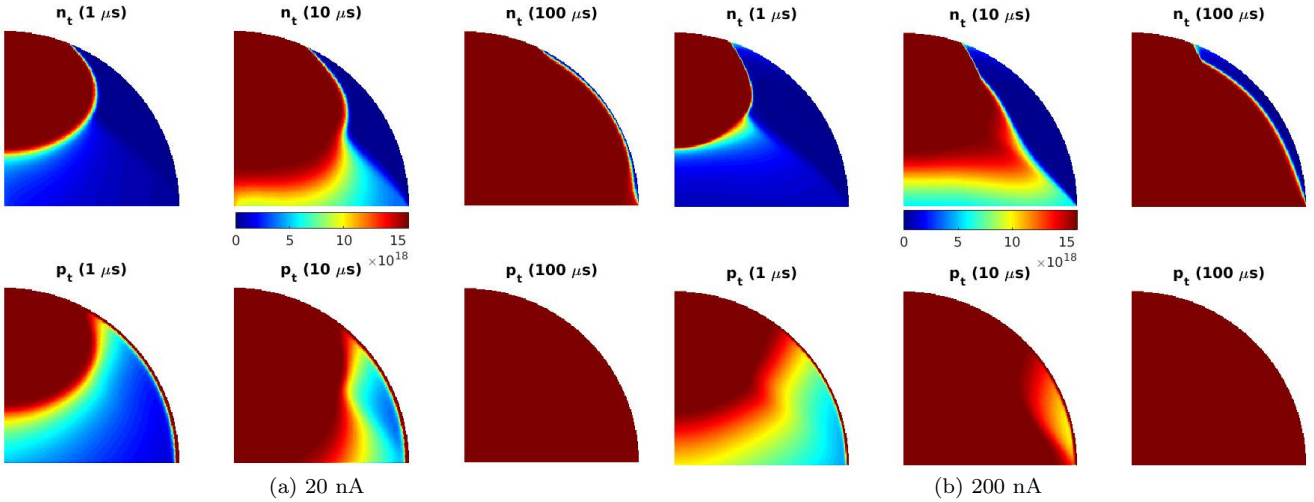

(a) 20 nA (b) 200 nA

FIG. 3. Densities of trapped electrons (top row) and trapped holes (bottom row) in Al_2O_3 half-sphere at 1, 10, and 100 μs since the start of irradiation by focused 20 nA **(a)** and 200 nA **(b)** beams of 1 keV PE's. At this current/energy levels a stable shock emerges causing a layer free of trapped electrons along the upper surface.

the steady state the maximum densities of free electrons (always in the middle of the impact zone) reach the values of 1.31×10^{19}, 1.36×10^{20}, 1.33×10^{21} and 1.3×10^{22} cm^{-3} with the beam currents of 0.2, 2, 20, and 200 nA, respectively. For the free holes, the corresponding maximum densities are 2.57×10^{19}, 2.41×10^{20}, 2.52×10^{21} and 2.08×10^{22} cm^{-3}, and are always found at the sample surface close the injection point. The electrostatic potential is weakly negative in the very early stages [up to 1 μs], after which it becomes predominantly positive throughout the sample, with the highest values of 1, 4, 17 and 28 V in the steady state for the aforementioned beam currents.

These results demonstrate a direct correlation between the magnitude of the beam current and the shock phenomenon and it can be concluded that the local charge concentration in the impact zone is a major factor, if not the only one, causing the shock.

To assess whether it is simply the mass production of secondary charge pairs that creates the lateral shock, simulations were carried out with the same high beam current of 200 nA and a higher PE energy of 5 keV. In this case, even more SE's are produced on each PE impact, and the total amount of generated charge increases. At the same time the pair production zone of 5 keV PE's is significantly larger than that of 1 keV PE's, which reduces the local concentration of free charge in the impact zone. Simulation does not show any shock in this case,

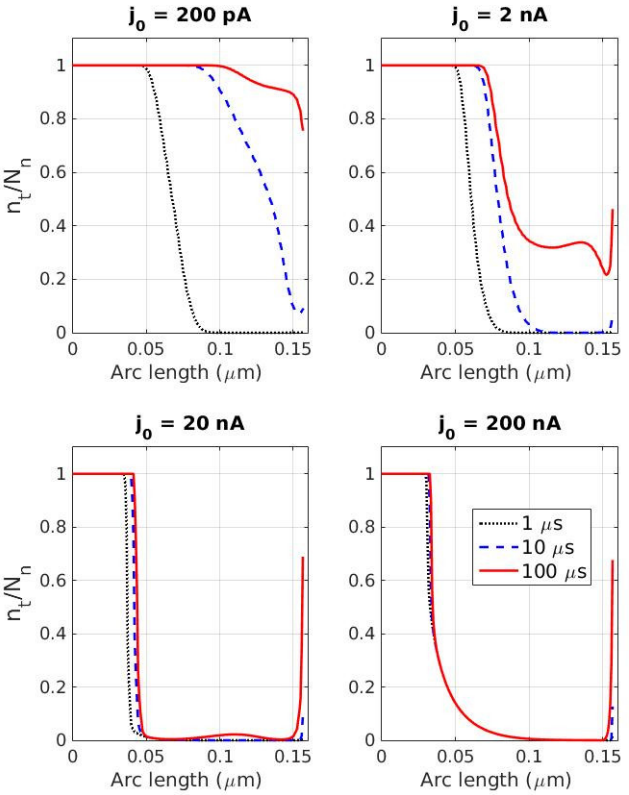

FIG. 4. Relative density of trapped electrons, n_t/N_n, at the surface of Al_2O_3 half-sphere (arc length is measured from top down) at 1, 10, and 100 μs after the start of irradiation with different beam currents. The energy of PE's is 1 keV and the SRV is 200 cm/s.

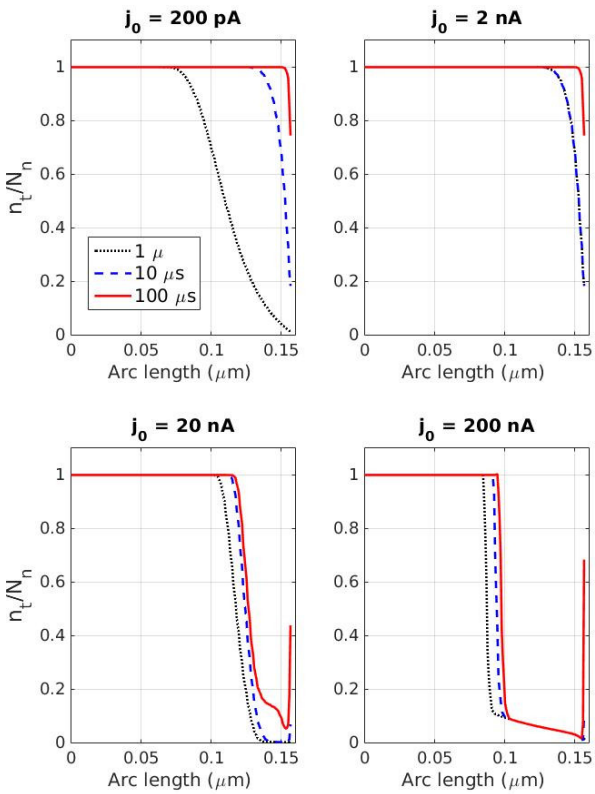

FIG. 5. Relative density of trapped electrons, n_t/N_n, at the surface of SiO_2 half-sphere (arc length is measured from top down) at 1, 10, and 100 μs after the start of irradiation with different beam currents. The energy of PE's is 1 keV and the SRV is 100 cm/s.

and all trapping sites of the insulating part are fully occupied by the trapped charges already in the early stages of irradiation. Thus, we can infer that the local charge concentration, i.e., the spatial gradient of charge density, rather than the total amount of charge is the major factor of influence in producing lateral shocks. Side note: both the free holes and the free electrons appear to reach the same maximal concentration of 1.49×10^{20} cm^{-3} with a 200 nA beam of 5 keV PE's.

B. Influence of material and shape

To confirm that lateral shocks are not limited to alumina we have considered a SiO_2 half-sphere of the same size irradiated by a 200 nA current of 1 keV PE's. Silica has material properties similar to those of alumina except for the density, dielectric constant, and the SRV, which for silica are all smaller then the corresponding parameters of alumina. Figure 5 shows the snapshots of the relative density of trapped electrons at the surface of SiO_2 half-sphere. The shock emerges here too, however, at higher beam currents, and its boundary is further from the injection point.

This indicates that the SRV may be an important parameter, since it is twice smaller in the case of SiO_2. SRV is definitely an important parameter when it comes to the SE yield. The yield of Al_2O_3 is known to vary greatly depending on the surface processing technique[39–41]. Our simulations indicate that the SRV of Al_2O_3 that provides the corresponding yields may vary between 100 and 1000 cm/s. Figure 6 shows that a moderate shock can emerge even with beam currents as small as 2 nA in materials with higher SRV's. Finally, Figure 7, where we consider an alumina cylinder, instead of a half-sphere, illustrates that the shock may exist in samples of various shapes.

C. Possible detection strategy

According to the above simulations the shock in the trapped-electron density will be observed in insulators with sufficiently high SRV's irradiated by a high-current well-focused beam of relatively low-energy electrons. The internal distribution of trapped-charge densities is hardly accessible in an experiment. Nevertheless, it should be possible to verify the existence of shocks by observing the surface of a sample. Since the shock zone is virtually free of electrons, the trapped holes will not be neutralized

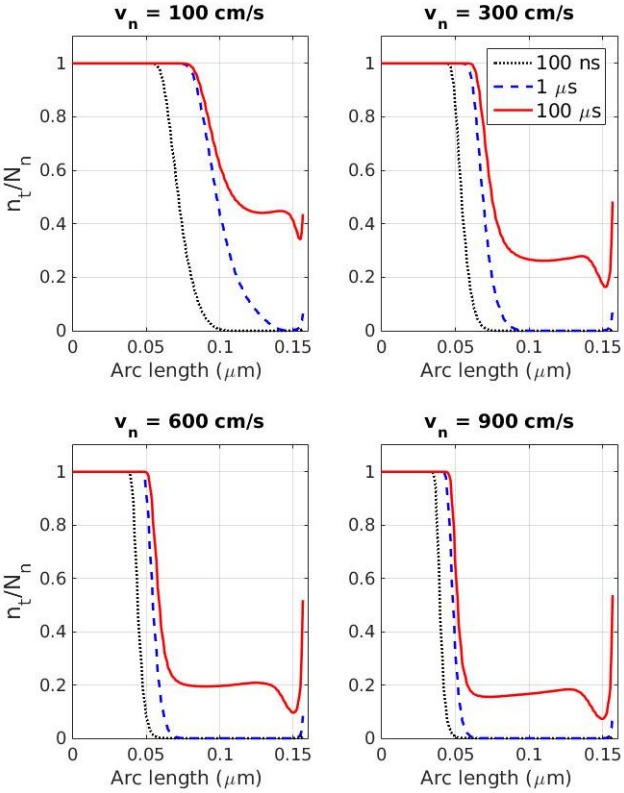

FIG. 6. Relative density of trapped electrons, n_t/N_n, at the surface of Al_2O_3 half-spheres characterized by different SRV's at 1, 10, and 100 μs after the start of irradiation with the beam current of 2 nA of 1 keV PE's.

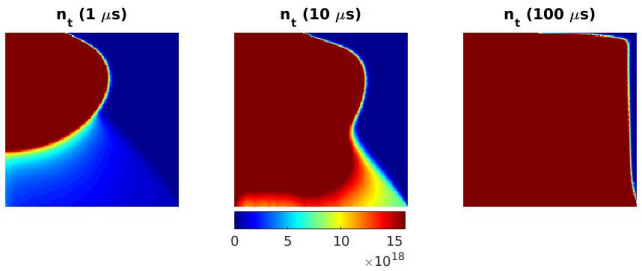

FIG. 7. Densities of trapped electrons in Al_2O_3 cylinder at 1, 10, and 100 μs since the start of irradiation by a focused 20 nA beam of 1 keV PE's.

providing a significant positive charge in that particular subsurface area. It is known that the rate of detrapping may be very low, meaning that any trapped charges will remain trapped for a very long time. Thus, the trapped holes inside the shock zone will be contributing to the total residual charge of the sample long after the electron beam has been switched off.

Figure 8 (a)–(c) shows the residual total charge on the alumina half-sphere 1, 2, and 10 μs after the beam, which was irradiating the sample for 10 μs, has been switched off. While the initial excess of free holes in the neighborhood of the injection point is removed by transport

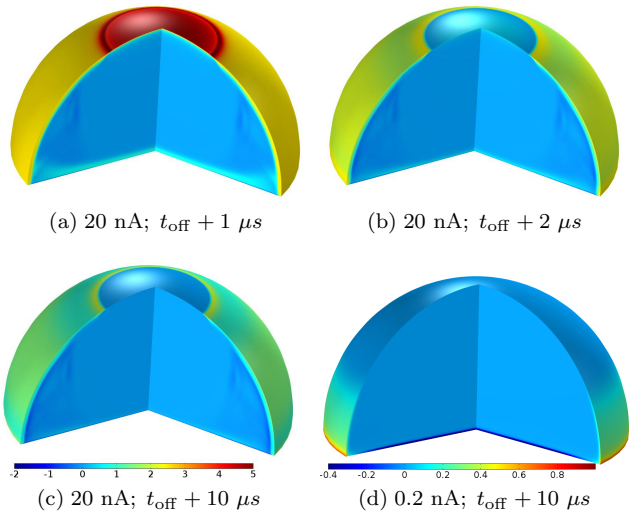

(a) 20 nA; $t_{\text{off}} + 1\ \mu s$ (b) 20 nA; $t_{\text{off}} + 2\ \mu s$

(c) 20 nA; $t_{\text{off}} + 10\ \mu s$ (d) 0.2 nA; $t_{\text{off}} + 10\ \mu s$

FIG. 8. Total charge density, [C/cm^3], in the alumina half-sphere after the beam has been switched off. (a)-(c): 20 nA beam current – shock is visible in both the shape and the strength of the residual surface charge; (d): 0.2 nA beam current – no shock, weaker residual surface charge. PE's energy is 1 keV, and the beam has been switched on for 10 μs.

and recombination within the first two microseconds, the surface above the shock zone remains positively charged for a much longer time, which may provide an opportunity for the detection/visualization of the shock. For comparison, Fig. 8 (d) shows the residual total charge in the same half-sphere after it was irradiated by a lower-current beam, which did not lead to the shock. The residual surface charge is approximately two times lower and has a very different distribution in the latter case.

IV. CHARGING AND YIELD VARIATIONS

The DDR method delivers good fits to experimental SE yield curves by tuning a single parameter – the SRV of the sample-vacuum interface. For instance, Fig. 9 shows comparison with both the experimental data[36] (reported also in the database of Joy[42]) and the Monte Carlo simulations[43] for an alumina sample. The tuned SRV value for the vacuum-alumina interface obtained by fitting the SE yield at 750 keV turns out to be 600 and 950 cm/s for unpolished and polished surfaces, respectively. This indicates that the SRV may be a highly varying parameter depending on both the material and the surface properties. Therefore, in subsequent numerical experiments we shall be employing a range of SRV values for alumina and silica samples, where the SRV of alumina is generally larger than the SRV of silica.

Reproduction of experimental results from dielectric samples remains a significant challenge, since the SE yield appears to be both not well-defined and unstable. For example, the yield-energy curves for sapphire pub-

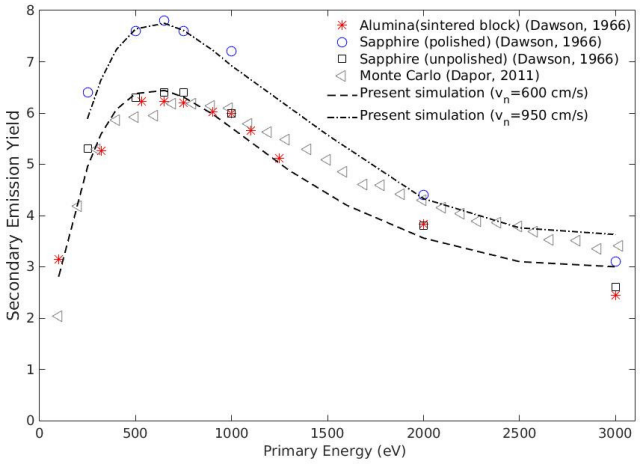

FIG. 9. SE yield for alumina as a function of PE energy. Comparison between the experimental data[36], the present DDR method, and the Monte Carlo technique[43].

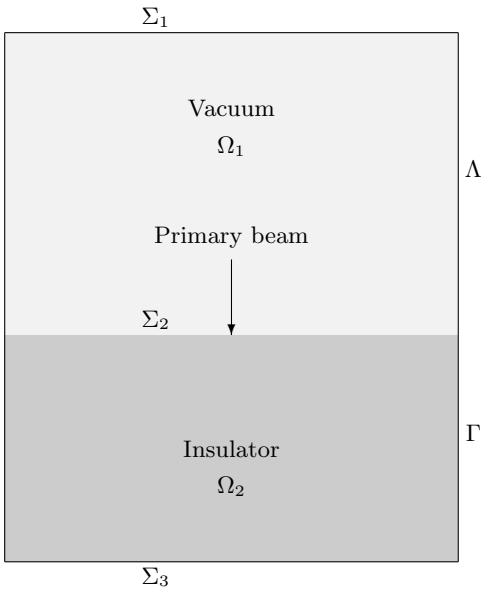

FIG. 10. Cross-section of the cylindrical dielectric sample considered in Section IV.

lished in[36],[44], and[45] reveal a clear discrepancy not only in the maxima but also in the overall shape of the curves. Also, the SEM images of insulators can either become overly dark or, on the contrary, 'overexposed', i.e., bright. Sometimes, the bright portion turns into a mirror that reflects an image of the SEM chamber interior (mirroring effect).

The problem stems from the lack of uniformity in the sample preparation (e.g. surface quality that affects the SRV), measurement protocols, and even the definition of the SE yield. One approach, for instance, employed in the classical study[36] (see Fig. 9), involves switching the primary 10 nA beam for a short period of time (~ 1 μs) and recording the received SE current pulse with an oscilloscope. Subsequently, these currents are integrated over time and the SE yield is computed as the ratio of the total injected primary charge to the total emitted secondary charge.

In the more recent SEM-based experiments[37,46] the measured quantity is the instantaneous current at the SE detector rather than the total emitted charge. The dynamic scanning of the sample with a focused PE beam means that the beam dwells only for a short period of time around a given injection point and the transient nature of the SE yield discussed below becomes more pronounced. Thus, a SEM-based yield measurement may give different results at different resolutions, since the scanning rate is typically kept constant (fixed number of frames per second), whereas the dwell time will vary depending on the zoom factor.

This section presents a systematic computational analysis of these SE yield variations, typically attributed to sample charging. For simplicity, a cylindrical sample (irradiated at its center) with cross-section shown in Fig. 10 will be considered in all simulations. As before, the boundary Σ_2 is the semi-permeable sample-vacuum interface characterized by its free-electron SRV. The lower boundary Σ_3 is non-penetrable to charge, which is achieved by fixing the gradients of the potential and free charge densities to be zeros at Σ_3. Depending on the simulation the side boundary Γ is either an ohmic contact, or a Schottky contact characterized by free-electron and free-hole SRV values, or an insulating boundary similar to Σ_3. The upper boundary Σ_1 is situated in vacuum and features a fixed potential $V = 0$ in all simulations, which is essential for the numerical stability of our solver.

To demonstrate that the actual SE yield is a time-dependent quantity with vastly different values in the beginning of the irradiation process and in the steady-state regime, in our subsequent numerical experiments we shall be focusing on the instantaneous yield defined as the ratio of PE and SE currents.

A. Early-time yield spike

Transient processes preceding the establishment of the steady-state regime may last anywhere from several microseconds to milliseconds and even seconds, depending on the sample size and bulk parameters. A truly steady-state regime is only achieved when there are no more changes in the local trapping rates. As shown in the previous section, if the current is not too high, then the trapped charge distribution tends to uniformly saturated trapping sites throughout the whole sample. The saturation process, however, is slow, which must be one of the reasons for the prolonged duration of the transient stage.

For the relatively small (less than 1 μm in diameter) grounded alumina and silica samples one can distinguish three main stages in the time evolution of the yield: a

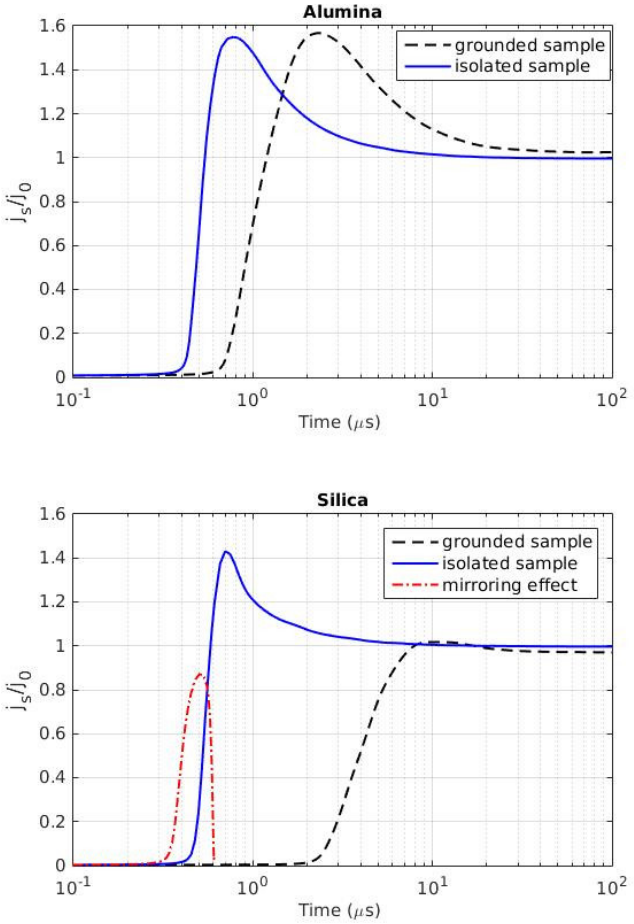

FIG. 11. Time evolution of the yield in grounded and isolated alumina and silica samples. The samples with the height and radius of 0.5 μm are irradiated by a 200 pA current of 5 keV PE's. The grounded Σ_1 contact (where $V = 0$) is 1 mm above the vacuum-sample interface Σ_2 (see Fig. 10). The electrostatic mirroring effect (dashed-and-dotted curve in the bottom plot) occurs in silica when the distance between Σ_1 and Σ_2 is 1.5 mm.

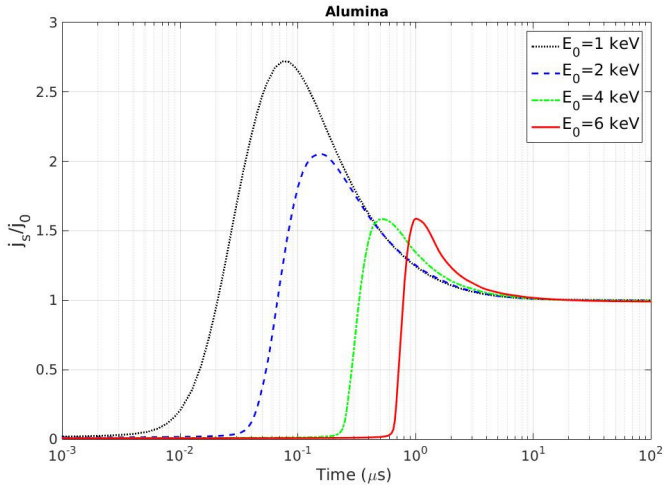

FIG. 12. Time evolution of the yield from an isolated alumina sample versus PE energy for a 200 pA beam current. The distance between Σ_1 and Σ_2 is 1 mm.

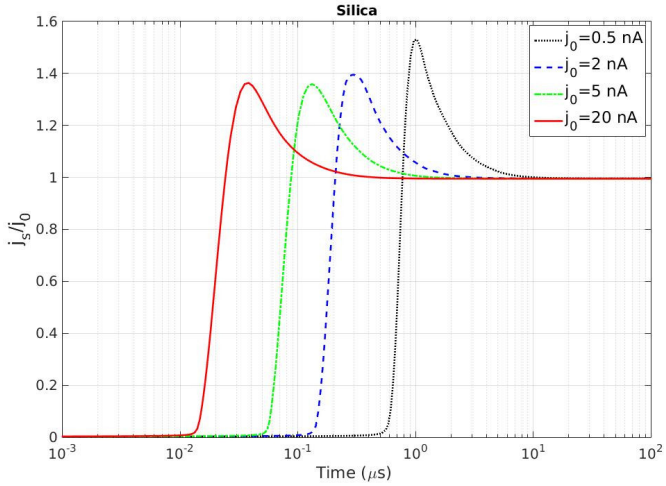

FIG. 13. Time evolution of the yield from an isolated silica sample for 5 eV PE energy versus the beam current. The distance between Σ_1 and Σ_2 is 0.1 mm.

rapid growth of the yield around $0 \leq t \leq 10$ μs, either temporary (grounded samples) or permanent (isolated samples) drop in the yield around $10 \leq t \leq 100$ μs, an increase in the yield in grounded samples and the establishment of the steady state 100 μs $\leq t \leq$ 100 ms.

As can be seen in Fig's 11, 12, and 13, at the beginning of the irradiation process the yield is always very small and it takes from 10 to 100 ns for it to start growing. Then, in all considered cases, apart from those where the mirroring effect has occurred, the yield rapidly climbs above unity. This increase in yield is temporary, lasting for a few microseconds, after which the yield drops either down to unity in isolated samples or to a certain quasi-stationary value above or below unity in grounded samples. The differences between the grounded and isolated samples will be studied and elaborated upon in the following sub-section. Here we focus on the common features of the early-time yield spike.

From Fig's. 12 and 13, where isolated alumina ans silica samples are considered, we observe that the low-yield period is shorter for lower energies and higher currents and longer for higher energies and lower currents. Since the current through the sample-vacuum interface is completely determined by the concentration of free electrons at the interface, the yield is low whenever the concentration of free secondary electrons at the surface is low. Dependencies of Fig's. 12 and 13 agree with the general properties of SE clouds generated upon the impact of PE's at different energies. The low-energy electrons create SE clouds closer to the interface, so the concentration of free electrons at the surface grows faster at lower energies and higher currents.

The reasons behind the yield climbing above unity are harder to ascertain. This transient spike in the yield oc-

curs in both grounded and isolated samples. We observe that in grounded samples the spike happens later than in isolated samples, see Fig. 11. Further, the spike in isolated samples is smaller at higher energies and slightly smaller at higher currents. Also, in many cases the spike in grounded samples is much smaller than in isolated ones, under the same irradiation conditions (see Fig. 11, bottom).

One can be sure that, at least in the isolated case, the spike cannot be caused by the additional inflow of electrons from the ground contact. Hence, we may hypothesize that it is caused by the temporary accumulation of injected primary and generated secondary electrons. This accumulation in its turn may be caused by the generally weak transport of particles in insulators away from the impact zone. Primary electrons have also something to do with it. To ascertain their role we have performed additional numerical experiments, where the contribution of the primary electron was removed from the source distribution function (9) by setting $B = 0$. In that case the yield, although initially grows, does not increase beyond unity and (in isolated samples) drops to zero after a few microseconds.

At higher beam currents the accumulation of free electrons at the sample-vacuum interface may be somewhat less significant, since both the drift and diffusion currents grow stronger in proportion to the concentration of charge in the impact zone. Hence, the rate at which the excess electrons are transported away from the impact zone and the sample-vacuum interface may become higher than the rate at which they are accumulated. Transient changes in the generation-recombination and trapping rates may also play roles that, however, will require many more dedicated numerical experiments to understand.

The significant drop in the yield after the spike is probably due to the following reasons. The holes cannot penetrate the sample-vacuum interface, only free electrons can. Hence, there will be a (temporary) excess of holes below the sample surface. This will increase the local recombination rate for the free electrons and reduce the current through the interface. In other words, electrons have less chance to reach the interface because they are captured by the large amount of holes just below the surface.

The importance of the transient yield spike stems from the fact that it is observed in both grounded and isolated samples. Its duration (in the order of microseconds) corresponds to the irradiation and measurement times in the classical experiment[36] and may be close to the dwell times in SEM-based yield measurements, where the relatively short duration of the spike may be responsible for the variations in image brightness.

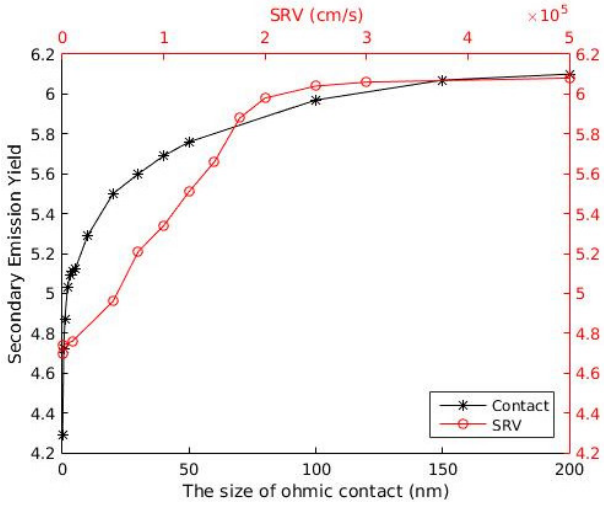

FIG. 14. The steady-state yield of Al_2O_3 as a function of the size of ohmic contact and SRV at the sample/conductor interface (Γ in Fig. 10). The PE energy, the beam current and the SRV at the vacuum-sample interface are 1 keV, 200 pA and 350 cm/s, respectively.

B. Quality of the ground contact

Whereas the early-time yield spike is caused by the temporary excess of PE's and SE's, a prolonged (quasi-stationary or steady-state) increase of the yield requires an additional sustained source of electrons. Hence, the type and the quality of the contact between the dielectric sample and the electrical ground should be a major factor influencing the yield after its initial spike.

To test this hypothesis we have considered samples with an ohmic side contact of a varying width, as measured from the top down along the Γ interface in Fig. 10, expecting that a smaller contact would restrict the flow of electrons/holes. In addition we have simulated a Schottky-type side contact at Γ with a varying SRV, expecting that a smaller SRV would restrict the flow of electrons/holes as well. As can be seen in Fig. 14 both of these changes do indeed cause a consistent drop in the steady-state yield.

As a limiting case we model a complete isolation of a sample as the zero Neumann boundary conditions for both the potential and the charge densities at Σ_3 and Γ, which prevents drift and diffusion currents through these interfaces. Apart from the extreme 'mirroring' situations described in the next sub-section, in the isolated case the yield drops exactly to unity and stays that way independently of the PE energy (see Fig. 12). Figure 13 shows that the convergence of the yield to unity is also independent of the beam current (for moderate currents). This agrees with the general charge conservation law, provided that the generation, recombination, and trapping/de-trapping rates are all balanced out from the equation. If the sample is isolated, then in the steady state one extra primary electron is injected (per unit of

time) and at the same time exactly one SE is expelled through the only available penetrable interface.

C. Surface potential and the mirroring effect

It is often claimed that the surface electric potential is the main cause of yield distortions in insulators. For example, the drop of yield to unity is believed to be caused by either the positive (at low PE energies) or negative (at higher PE energies) charging of the sample, which increases/reduces the landing energy of primary electrons until it reaches one of the two points where the 'normal' (uncharged) yield curve crosses the unity line[48,49]. Although, in principle, this is possible, since the steady-state charge conservation in isolated samples does not mean that the internal charge distribution is uniform or even neutral and a significant amount of charge can accumulate and be maintained in the sample in the steady state, yet, so far, we were not able to confirm the simple charging models proposed in[48,49].

In our numerical experiments grounded samples have never shown any significant surface potential. However, the value of potential on the surface of isolated samples can easily reach several kilovolts. Figure 15 presents the time evolution of the potential at the injection point in isolated alumina and silica samples for a 200 pA beam of 5 keV PE's. In alumina the potential initially drops below zero reaching -1.6 keV right around the time when the yield attains its maximum (see Fig. 11), but then it starts to increase and becomes positive reaching approximately 2.5 keV. These positive potentials at the alumina surface are in agreement with previously reported experimental observations[47]. In silica the potential drops significantly below zero, but then returns to almost zero, thus, having no influence on the PE landing energy in the interstage.

Apparently, the most important parameter controlling the magnitude of the potential is not the total charge density, as one would naively assume, but the distance to the closest Dirichlet boundary (where the electric potential is maintained at some fixed value, e.g., zero). In our simulations this is either the Σ_1 boundary or the ohmic contact Γ, if the sample is grounded. The different curves in Fig. 15 correspond to different distances between Σ_1 and the sample-vacuum interface Σ_2. We stress that in all these cases the yield has converged to unity after the initial spike, since the sample is isolated.

As one can see, the magnitude of deviations in the potential V grows with the distance to the ground contact. In fact, in silica when the distance increases beyond 1.5 mm the potential at the injection point can drop to -5 keV making the landing energy of the 5 keV PE's exactly zero. In this case the primary electrons will start bouncing off the sample surface. We believe that this reproduces the so-called mirroring effect, often observed in SEM studies of insulators. The corresponding time evolution of the yield is shown as dashed-and-dotted curve in Fig. 11.

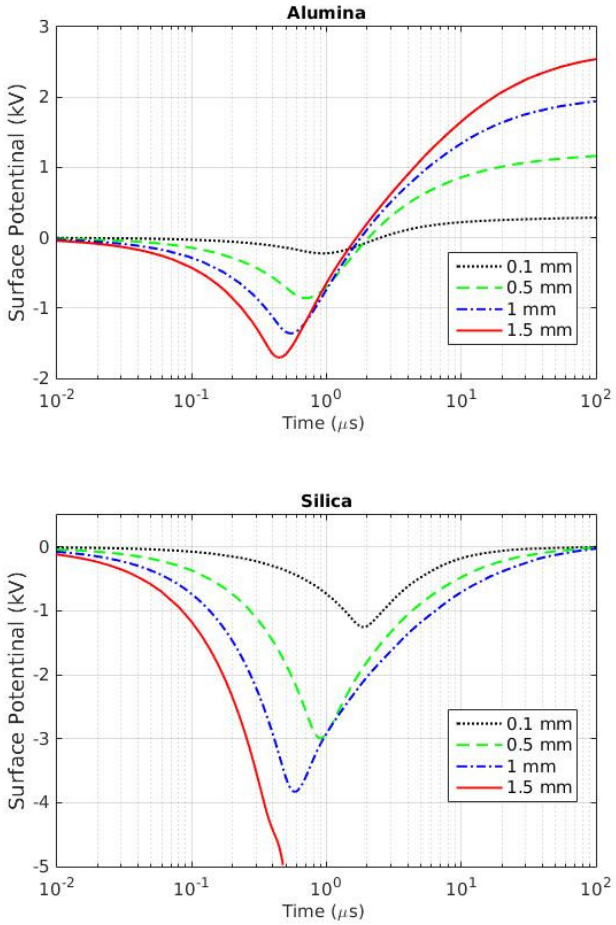

FIG. 15. Time evolution of the electric potential at the injection point versus the distance to the nearest grounded contact (i.e. distance between Σ_1 and Σ_2, see Fig. 10). Same isolated samples and irradiation conditions as in Fig. 11.

Figure 16 explicitly shows that the total charge in both grounded and isolated alumina samples at 1 μs is of the same order and has similar distributions. Notably, although the potential at the injection point is negative, there is a significant amount of positive charge inside the sample, with the negative charge concentrated mostly at the surface. The bottom plots of Fig. 16 show that the presence of a close Dirichlet boundary (i.e. the ohmic contact Γ of the grounded sample) significantly reduces the magnitude of the resulting potential along the sample-vacuum interface Σ_2, including the injection point. In other words, the same amount of charge will produce vastly different potentials depending on the proximity of an ohmic contact. Physically, this could be viewed as the screening of the charges in the sample by the charges inside the (metallic) ground electrode.

The magnitude of transient potential deviations at the injection point depends on the PE energy as well – the larger the energy the larger the deviations, see Fig. 17. However, the mirroring effect in silica is only observed for

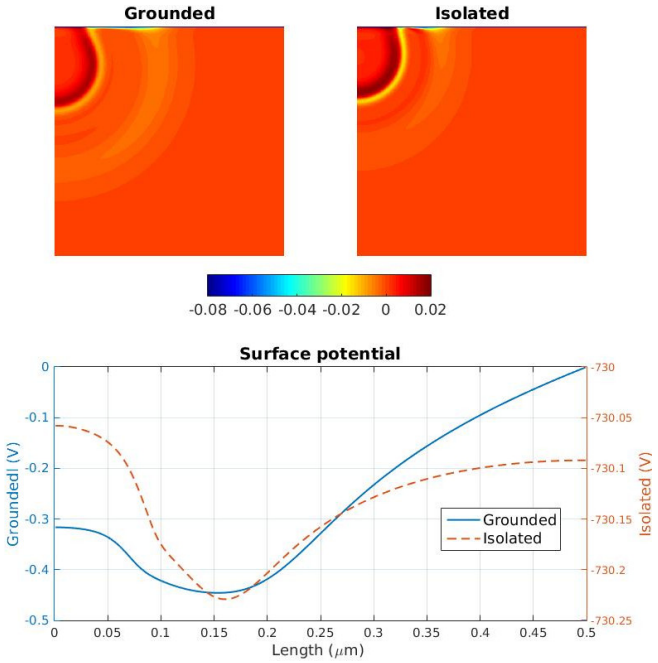

FIG. 16. Total charge density [C/cm^3] (top) and the surface potential (bottom) in grounded and isolated alumina samples at 1 μs since the start of irradiation with a 200 pA beam of 5 keV PE's. The distance between Σ_1 and Σ_2 is 1 mm in both cases.

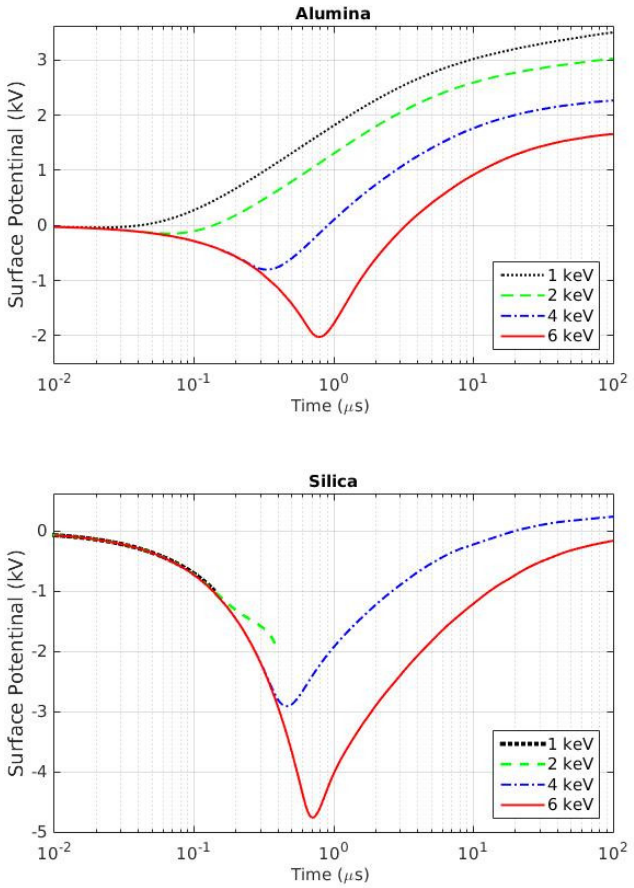

FIG. 17. Time evolution of the electric potential at the injection point versus the PE energy in isolated alumina and silica samples. Same samples and irradiation conditions as in Fig. 11. The distance between Σ_1 and Σ_2 is 1 mm in both cases.

PE's with energies below 2 keV, as for higher PE energies the potential deviations are not strong enough (for the ground contact at 1 mm).

The mirroring effect is stable in the sense that once the landing energy of PE's becomes zero, the corresponding critical potential is maintained in the sample for a very long time. This indicates (and was confirmed by the inspection of charge density plots) that the critical potential is caused by the trapped rather than free charges.

Interestingly, the mirroring effect was not observed in the considered isolated alumina sample no matter how large the distance to the grounded contact or how small the PE energy. It turns out that in addition to the ground proximity and PE's energy the other parameter controlling the possibility of the mirroring effect is the dielectric permittivity ε of the material, which is higher in alumina. A larger ε reduces the electric field inside the sample.

D. Steady-state yield

While in isolated samples the yield converges to either unity or zero (mirroring effect), in grounded samples the yield generally recovers after its drop following the initial spike. We attribute this difference to the establishment of a free-electron current from the ohmic contact to the sample-vacuum interface and the complete saturation of all traps.

Figure 18 confirms this hypothesis by comparing the yield evolution in samples with and without trapping. When all traps are saturated, the trapping rate is either zero or a very small negative number (de-trapping is extremely slow). Hence, a sample with saturated traps behaves almost exactly like a sample without trapping. That is why the two curves coincide when the steady state is reached in the sample with trapping. Notably, this true steady sate is achieved rather late, around 100 ms, even in the relatively small sample considered here.

In samples without trapping, however, the same steady-state yield is established much sooner, around 1 μs. The latter fact allows for significant simplification of the steady-state yield computations in trap-saturated grounded samples by simply omitting the trapping effect altogether. In this way one can perform much faster simulations on much larger samples. For example, Fig. 19 shows that the steady-state yield of alumina as a function of PE energy (for a sample with 200 nm radius and height) computed using the slow code with trapping effect included (circles) coincides – for a wide range of PE energies – with the fast computation that neglects trap-

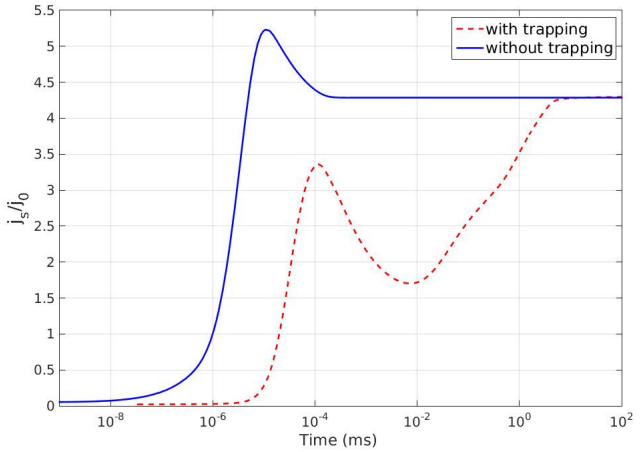

FIG. 18. The evolution of yield with and without trapping effect for alumina with a 200 pA beam of 1 keV PE's.

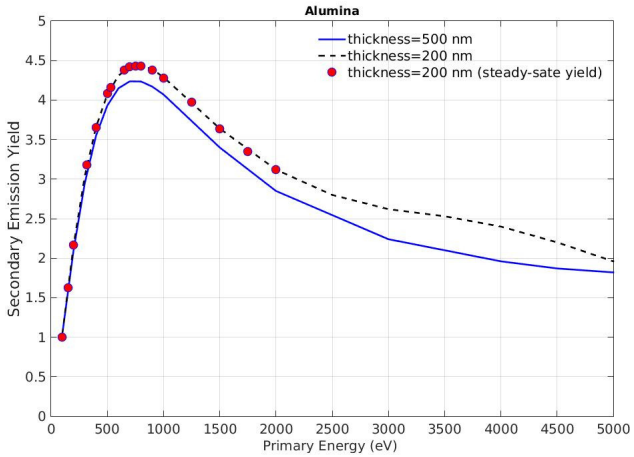

FIG. 19. The steady-state yield of alumina for samples of different size. Curves show fast computations that neglect the trapping process. Circles correspond to slow computations with the trapping process included. The beam current is 200 pA and the SRV is 200 cm/s.

ping (dashed curve). The solid curve in Fig. 19 shows the steady-state SE-yield for a sample with 500 nm radius and height computed with the fast algorithm that neglects trapping. Apparently, the yield is slightly lower in a larger sample. However, our simulations show that this effect saturates if the sample size is increased even further.

Finally, Fig. 20 demonstrates the dependence of the steady-state yield in alumina on the PE current. In general, the steady-state yield growth with the beam current, especially at low current values characteristic of SEM. The yield at lower energies is more sensitive to the current changes than at higher energies.

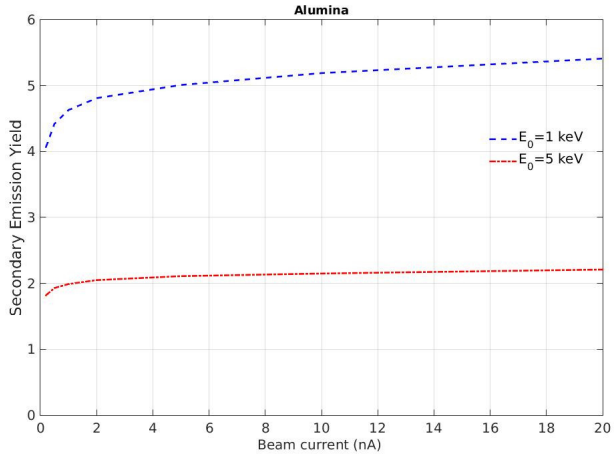

FIG. 20. The steady-state yield of alumina with the primary energies of 1 and 5 keV as a function of beam current.

V. CONCLUSIONS

The DDR method proposed in[22] and further elaborated here is a viable alternative to Monte Carlo simulations of electron-beam irradiated insulators. Numerical simulations presented above show that this method not only reproduces various well-known effects, but allows to ascertain their causes and discover new phenomena as well.

In particular, it was shown that a quasi-stationary lateral shock in the trapped-electrons density may emerge in samples irradiated by highly focused low-energy beams. In practice, it may be difficult to achieve the desired degree of focusing. Yet, the subsurface ring-shaped layer surrounding the impact zone featuring a significant excess of trapped holes with respect to trapped electrons may temporarily emerge and, possibly, be detected under much weaker conditions.

Our numerical experiments demonstrate that including the trapping effect is essential if rapid scanning or other early-time processes are to be simulated. However, as we have found out, the trapping can be neglected when simulating the steady state, significantly simplifying and speeding up the calculations. A good ground contact is crucial for higher steady-state yields. However, the early-time yield spike occurs in both grounded and isolated samples and may be the reason for relatively high, but unstable yields observed in SEM studies of insulators.

A simple grounded metal pin close to the beam injection point may significantly reduce the electric potential of the trapped charge and the associated distortions in the landing energy of PE's. Changing the proximity of a grounded (metal) contact may also be a means to control the relative importance of the drift current with respect to the diffusion current in the transport of charged particles.

A recent review by Walker et al[15] mentions the lack of reliable simulations related to low-energy SEM studies.

The DDR approach partly fills this gap and may be useful in investigating the influence of the scanning speed, beam current, and the quality of ground contact on the SEM images of insulators, allowing for long-time and large-volume simulations.

ACKNOWLEDGEMENTS

The authors acknowledge the partial financial support of the FEI Company (Netherlands) and many fruitful discussions with Prof. H. van der Graaf, Cornelis W. Hagen, Shuxia Tao, Anne M.M.G. Theulings and Hong Wah Chan (all from Charged Particle Optics group at Delft University of Technology).

[1]AD Bass, P Cloutier and L Sanche. Measurements of charge accumulation induced by monochromatic low-energy electrons at the surface of insulating samples. *Journal of applied physics*, 84(5), 2740–2748, 1998.

[2]JS Lee and J Cho and C Lee and I Kim and J Park and YM Kim and H Shin and J Lee and F Caruso. Layer-by-layer assembled charge-trap memory devices with adjustable electronic properties. *Nature nanotechnology*, 2(12), 790–795, 2007.

[3]BM Kulwicki and AJ Purdes. Diffusion potentials in BaTiO3 and the theory of PTC materials. *Ferroelectrics*, 1(1), 253–263, 1970.

[4]Vampola, AL and Mizera, PF and Koons, HC and Fennell, JF and Hall, DF. *The Aerospace Spacecraft Charging Document*. No. SD-TR-0084A (5940-05)-10. AEROSPACE CORP EL SEGUNDO CA LAB OPERATIONS, 1985.

[5]B Gross. Irradiation effects in borosilicate glass. *Physical Review*, 107(2), 368–374, 1957.

[6]B Gross. Irradiation effects in Plexiglas. *Journal of Polymer Science*, 27(115), 135–143, 1958.

[7]B Gross and S.V Nablo. High Potentials in Electron-Irradiated Dielectrics. *Journal of Applied Physics*, 38(5), 2272–2275, 1967.

[8]B Gross, J Dow and S.V Nablo. Charge buildup in electron-irradiated dielectrics. *Journal of Applied Physics*, 44(6), 2459–2463, 1973.

[9]B Gross,GM Sessler and JE West. Charge dynamics for electron-irradiated polymer-foil electrets. *Journal of Applied Physics*, 45(7), 2841–2851, 1974.

[10]B Gross and LN de Oliveira. Transport of excess charge in electron-irradiated dielectrics. *Journal of Applied Physics*, 45(11), 4724–4729, 1974.

[11]R Le Bihan. Study of ferroelectric and ferroelastic domain structures by scanning electron microscopy. *Ferroelectrics*, 97(1), 19–46, 1989.

[12]H Liebl. SIMS instrumentation and imaging techniques. *Scanning*, 3(2), 79–89, 1980.

[13]X Meyza, D Goeuriot, C Guerret-Piécourt, D Tréheux and H-J Fitting. Secondary electron emission and self-consistent charge transport and storage in bulk insulators: Application to alumina. *Journal of applied physics*, 94(8), 5384–5392, 2003.

[14]M Touzin, D Goeuriot, C Guerret-Piécourt, D Juvé, D Tréheux and H-J Fitting. Electron beam charging of insulators: A self-consistent flight-drift model. *Journal of applied physics*, 99(11), 114110, 2006.

[15]GHC Walker, L Frank and I Müllerová. Simulations and measurements in scanning electron microscopes at low electron energy. *Scanning*, 9999, 1–17, 2016.

[16]Wei-Qin Li, Kun Mu and Rong-Hou Xia. Self-consistent charging in dielectric films under defocused electron beam irradiation. *Micron*, 42(5), 443–448, 2011.

[17]Wei-Qin Li and Hai-Bo Zhang. The surface potential of insulating thin films negatively charged by a low-energy focused electron beam. *Micron*, 41(5), 416–422, 2010.

[18]GF Dionne. Origin of secondary-electron-emission yield-curve parameters. *Journal of Applied Physics*, 46(8), 3347–3351, 1975.

[19]LB Henke, J Liesegang and SD Smith. Soft-x-ray-induced secondary-electron emission from semiconductors and insulators: Models and measurements. *Physical review B*, 19(6), 3004, 1979.

[20]AO Barut. The mechanism of secondary electron emission. *Physical Review*, 93(5), 981, 1954.

[21]E Kieft and E Bosch. Refinement of Monte Carlo simulations of electron–specimen interaction in low-voltage SE. *Journal of Physics D: Applied Physics*, 41(21), 215310, 2008.

[22]Raftari B and Budko NV and Vuik C. Self-consistent drift-diffusion-reaction model for the electron beam interaction with dielectric samples. *Journal of Applied Physics*, 118(20):204101, 2015.

[23]H-J Fitting, H Glaefeke, and W Wild. Electron penetration and energy transfer in solid targets. *physica status solidi (a)*, 43(1):185–190, 1977.

[24]PA Markowich, C Ringhofer, and C Schmeiser. *Semiconductor equations*. Springer-Verlag New York, Inc., 1990.

[25]H-J Fitting and M Touzin. Secondary electron emission and self-consistent charge transport in semi-insulating samples. *Journal of Applied Physics*, 110(4):044111, 2011.

[26]J Nakano, S Sridhar, J Bennett, K Kwong and T Moss. Interactions of refractory materials with molten gasifier slags. *International Journal of Hydrogen Energy*, 36(7), 4595–4604, 2011.

[27]IM Sadiq, S Pakrashi, N Chandrasekaran and A Mukherjee. Studies on toxicity of aluminum oxide (Al2O3) nanoparticles to microalgae species: Scenedesmus sp. and Chlorella sp. *Journal of Nanoparticle Research*, 13(8), 3287–3299, 2011.

[28]Jerome, Joseph W. Consistency of semiconductor modeling: an existence/stability analysis for the stationary van Roosbroeck system. *SIAM journal on applied mathematics*, 45(4): 565–590, 1985.

[29]Jerome, Joseph W. Modeling and analysis of laser-beam-induced current images in semiconductors. *SIAM journal on applied mathematics*, 53(1): 187–204, 1993.

[30]SJ Polak, C Den Heijer, WHA Schilders and P Markowich. Semiconductor device modelling from the numerical point of view. *International Journal for Numerical Methods in Engineering*, 24(4): 763–838, 1987.

[31]JHM Ten Thije Boonkkamp and WHA Schilders. An exponential fitting scheme for the electrothermal device equations specifically for the simulation of avalanche generation. *COMPEL-The international journal for computation and mathematics in electrical and electronic engineering*, 12(2): 95–111, 1993.

[32]P Bayle and B Cornebois. Propagation of ionizing electron shock waves in electrical breakdown. *Physical Review A*, 31(2): 1046–1058, 1985.

[33]P Bayle and I Abbas. Non-equilibrium between electrons and field in a gas breakdown ionising wave. I. Macroscopic model. *Physical Review A*, 31(2): 1046–1058, 1985.

[34]CL Gardner, JW Jerome and DJ Rose. Numerical methods for the hydrodynamic device model: subsonic flow. *IEEE Transactions on Computer-Aided Design of Integrated Circuits and Systems*, 8(5), 501–507, 1989.

[35]CL Gardner. Numerical simulation of a steady-state electron shock wave in a submicrometer semiconductor device. *IEEE Transactions on Electron Devices*, 38(2), 392–398, 1991.

[36]PH Dawson. Secondary electron emission yields of some ceramics. *Journal of Applied Physics*, 37(9), 3644–3645, 1966.

[37]S Fakhfakh, O Jbara, S Rondot, A Hadjadj and Z Fakhfakh. Experimental characterisation of charge distribution and transport in electron irradiated PMMA. *Journal of Non-Crystalline Solids*, 358(8), 1157–1164, 2012.

[38]Ichimura, Takashi and Ren, Yan and Kruit, P. A large current scanning electron microscope with MEMS-based multi-beam optics *Microelectronic Engineering*, 113: 109–113, 2014.

[39]L.L. Rosier. Surface state and surface recombination velocity characteristics of Si-SiO 2 interfaces. *Electron Devices, IEEE Transactions on*, (2), 260–268, 1966.

[40]D Baek, S Rouvimov, B Kim, T-C Jo and DK Schroder. Surface recombination velocity of silicon wafers by photoluminescence. *Applied Physics Letters*, 86(11), 112110, 2005.

[41]B Imangholi, F.L. Lie, H.G. Parks and A.J. Muscat. Effect of deep-level defects on surface recombination velocity at the interface between silicon and dielectric films. *Electron Devices, IEEE Transactions on*, 57(4), 877–889, 2010.

[42]DC Joy. A database of electron-solid interactions, revision 08-1, 2008.

[43]M Dapor. Secondary electron emission yield calculation performed using two different Monte Carlo strategies. *Nuclear Instruments and Methods in Physics Research Section B: Beam Interactions with Materials and Atoms*, 269(14), 1668–1671, 2011.

[44]S Michizono, Y Saito, S Yamaguchi, S Anami, N Matuda and A Kinbara, A. Dielectric materials for use as output window in high-power klystrons. *IEEE transactions on electrical insulation*, 28(4), 692–699, 1993.

[45]J Barnard, I Bojko, and N Hilleret. Measurements of the secondary electron emission of some insulators. *Internal Note (CERN)*, 1997.

[46]K Said, G Damamme, A Si Ahmed, G Moya, A Kallel. Dependence of secondary electron emission on surface charging in sapphire and polycrystalline alumina: Evaluation of the effective cross sections for recombination and trapping. *Applied Surface Science*, 297, 45–51, 2014.

[47]O Jbara, M Belhaj, S Odof, K Msellak, EI Rau and MV Andrianov. Surface potential measurements of electron-irradiated insulators using backscattered and secondary electron spectra from an electrostatic toroidal spectrometer adapted for scanning electron microscope applications. *Review Of Scientific Instruments*, 72(3), 1788–1795, 2001.

[48]R Renoud, F Mady, C Attard, J Bigarre, J-P Ganachaud. Secondary electron emission of an insulating target induced by a well-focused electron beam–Monte Carlo simulation study. *physica status solidi (a)*, 201(9), 2119–2133, 2004.

[49]M Touzin, D Goeuriot, C Guerret-Piécourt, D Juvé, D Tréheux and H-J Fitting. Electron beam charging of insulators: A self-consistent flight-drift model. *Journal of applied physics*, 99(11), 114110, 2006.